# Pulse Density Modulation for Maximum Efficiency Point Tracking of Wireless Power Transfer Systems

Hongchang Li, *Member, IEEE*, Jingyang Fang, *Student Member, IEEE*, Shuxin Chen, *Student Member, IEEE*, Kangping Wang, *Student Member, IEEE*, Yi Tang, *Member, IEEE*

***Abstract*—Maximum efficiency point tracking (MEPT) control has been adopted in state-of-the-art wireless power transfer (WPT) systems to meet the power demands with the highest efficiency against coupling and load variations. Conventional MEPT implementations use dc/dc converters on both transmitting and receiving sides to regulate the output voltage and maximize the system efficiency at the expense of increased overall complexity and power losses on the dc/dc converters. Other implementations use phase-shift control or on-off control of the transmitting side inverter and the receiving side active rectifier instead of dc/dc converters but cause new problems, e.g. hard switching, low average efficiency, and large dc voltage ripples. This paper proposes a pulse density modulation (PDM) based implementation for MEPT to eliminate all the mentioned disadvantages of existing implementations. Delta-sigma modulators are used as an example to realize the PDM. A dual-side soft switching technique is proposed for the PDM. The ripple factor of output voltage with PDM is derived out. A 50W WPT system is built to validate the proposed method. The system efficiency is maintained higher than 70% for various load resistances when the power transfer distance is 0.5m, which is 1.67 times the diameter of the coils.**

***Index Terms*—Dual-side soft switching, maximum efficiency point tracking (MEPT), pulse density modulation (PDM), wireless power transfer (WPT)**

## I. Introduction

THE coupling coefficient and the load resistance of a wireless power transfer (WPT) system are usually uncertain and varying in many applications, and both the two parameters affect the output power and the system efficiency significantly [2]. To provide the desired power with the highest efficiency, maximum efficiency point tracking (MEPT) control strategies were proposed and employed by state-of-the-art WPT systems [2-8], e.g. reference [2] showed that MEPT control can effectively improve system efficiency as compared with frequency control and primary side dc link voltage control.

Conventional MEPT implementations use a dc/dc converter on the transmitting side to linearly regulate the output voltage and another dc/dc converter on the receiving side to convert the equivalent load resistance to its optimal value that depends on the coupling so that the maximum theoretical efficiency is achieved [2]. From the efficiency point of view, this method is profitable only if the power loss on the receiving side dc/dc converter can be compensated by the efficiency increase of the WPT link (from the transmitting side inverter to the receiving side rectifier). Considering that the efficiency of a high-power density point-of-load converter is relatively low [9], the efficiency of conventional MEPT implementations may be limited by the receiving side dc/dc converters in point-of-load applications, e.g. cellphone chargers [10]. Other disadvantages of these implementations are the increased system complexity and the slower dynamic response due to the additional dc/dc converters and their time constants.

An alternative method to convert the equivalent load resistance to its optimal value is using a phase-shift active rectifier. In [11], a dual-side control method was proposed to regulate the output power and maximize the system efficiency by means of phase-shift control, which is like the control of dual active bridge converters. This method is also a candidate implementation of MEPT. However, the disadvantage is the hard switching caused by the phase shift. Because of the hard switching, the operating frequency of the prototype in [11] is as low as 35kHz, which is not high enough for large distance or loose coupling WPT applications, e.g. multiple-receiver systems [12] and dynamic electrical vehicle charging [13]. In these applications, the low mutual inductance must be compensated by a high operating frequency for sufficient power transfer capacity, and the low coupling coefficient must be compensated by high quality factors of the resonators for high power transfer efficiency. High quality factors also rely on a high operating frequency.

Besides, a secondary-side-only power and efficiency control method was proposed in [14, 15]. This method can be regarded

This work was supported by the Nanyang Technological University under Grant NTU-SUG M4081608. *(Corresponding author: Yi Tang)*

The original conference paper is [1] H. Li, J. Fang, and Y. Tang, "Delta-sigma modulation for maximum efficiency point tracking of wireless power transfer systems," in *2017 IEEE 3rd International Future Energy Electronics Conference and ECCE Asia (IFEEC 2017 - ECCE Asia)*, 2017, pp. 434-437.

Hongchang Li is with the Energy Research Institute @ NTU, Nanyang Technological University, Singapore (e-mail: hongchangli@ntu.edu.sg).

Jingyang Fang, Shuxin Chen, and Yi Tang are with the School of Electrical and Electronic Engineering, Nanyang Technological University, Singapore (e-mail: jyang006@e.ntu.edu.sg; chen1095@e.ntu.edu.sg; yitang@ntu.edu.sg).

Kangping Wang is with the School of Electrical Engineering, Xi'an Jiaotong University, Xi'an, China (e-mail: wangkangping@stu.xjtu.edu.cn).

as the third candidate implementation of MEPT. The power flow is controlled by a half-bridge active rectifier that operates in "rectification mode" and "short mode" alternately (on-off control). The equivalent load resistance is converted to its optimal value by a receiving side dc/dc converter. One advantage of this implementation is that both the power regulation and the efficiency maximization are performed on the receiving side so that the control does not rely on wireless communication links. The second advantage is that there is no dc/dc converter on the transmitting side. However, the maximum efficiency is achieved only during the "rectification mode", and the efficiency during the "short mode" is zero. Therefore, the average efficiency is lower [14]. Another disadvantage is the large dc voltage ripples caused by the very low frequency on-off operation of the active rectifier, because the on-off frequency must be much lower than the switching frequency of the dc/dc converter [14] to decouple the control of the active rectifier and the dc/dc converter. The same problem also exists in a recently proposed "On-Off Keying" method, which applies the on-off control on the transmitting side inverter [16].

Although MEPT is an attractive control strategy for WPT systems, existing MEPT implementations are not satisfactory. Therefore, this paper proposes a pulse density modulation (PDM) based implementation for MEPT as the fourth candidate. The motivation of this study is to eliminate all the mentioned disadvantages of the existing MEPT implementations.

Compared with pulse width modulation (PWM) and pulse frequency modulation (PFM), PDM is preferred by WPT systems because both soft switching and tuning in resonance are critical. Compared with other resonant converters, WPT systems are the most suitable applications for PDM because the loaded quality factors of WPT systems are much higher than those of other resonant converters. Because of this match, PDM was used in WPT systems for transmitting side voltage/power regulation in previous studies [17-20]. However, these studies did not present the theory or implementation of efficiency maximization. This paper applies PDM on both transmitting and receiving sides to perform not only voltage/power regulation but also efficiency maximization, and thus, comes up with the PDM for MEPT of WPT systems.

## II. Review of MEPT

The original idea of load matching for efficiency maximization of WPT was found in [21], which presented the formulas of power transfer capability, approximated split frequencies, figure-of-merit, and the optimal load based on the coupled-mode theory. Later, the formulas of the figure-of-merit, the optimal load, and the maximum theoretical efficiency were derived based on a lumped parameter ac equivalent circuit model [2]. This circuit model is shown in Fig. 1, where $L_1$, $C_1$, $R_1$ and $L_2$, $C_2$, $R_2$ are the inductance, capacitance, and equivalent series resistance (ESR) of the resonators on the two sides, respectively, $M$ is the mutual inductance of the coupled coils, $U_1$ is the fundamental component of the driving voltage, and $R_e$ is the equivalent load resistance.

Suppose the angular frequency of $U_1$ is $\omega_s$, and the angular

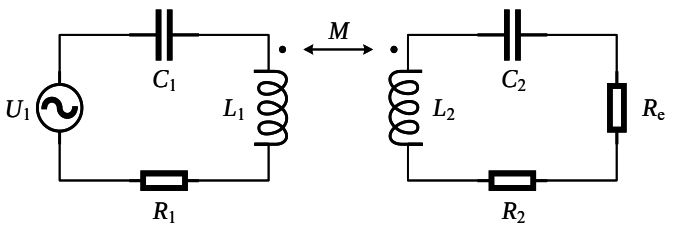


Fig. 1. Lumped parameter ac equivalent circuit model.

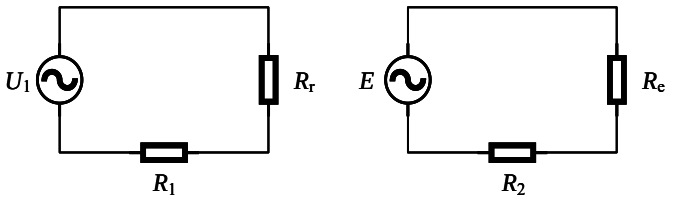


Fig. 2. Decoupled ac equivalent circuit.

resonant frequencies of the resonators on the two sides are $\omega_1$ and $\omega_2$, respectively. When the system is tuned in resonance, i.e.

$$\omega_s = \omega_1 = \omega_2 \tag{1}$$

Fig. 1 can be decoupled as Fig. 2, where $E$ is the induced voltage, and $R_r$ is the reflected resistance:

$$R_r = \frac{(\omega_s M)^2}{R_2 + R_e} \tag{2}$$

The power transfer efficiency $\eta$ is the product of the transmitting efficiency $\eta_1$ and the receiving efficiency $\eta_2$, i.e.

$$\eta = \eta_1 \times \eta_2 = \frac{R_r}{R_1 + R_r} \times \frac{R_e}{R_2 + R_e} \tag{3}$$

By setting the derivative of $\eta$ with respect to $R_e$ to zero, it can be found that there is an optimal $R_e$ that maximizes $\eta$ [22]:

$$R_{e\_optimal} = R_2 \sqrt{1 + fom^2} \tag{4}$$

where *fom* is the figure-of-merit, which can be expressed either by $\omega_s$, $M$, $R_1$, and $R_2$ or by the coupling coefficient $k$ and quality factors $Q_1$ and $Q_2$:

$$fom = \frac{\omega_s M}{\sqrt{R_1 R_2}} = k\sqrt{Q_1 Q_2} \tag{5}$$

The maximum theoretical efficiency is given by

$$\eta_{max} = 1 - \frac{2}{1 + \sqrt{1 + fom^2}} \tag{6}$$

When *fom* is large, (6) can be approximated to

$$\eta_{max} \approx \frac{fom - 1}{fom + 1} \tag{7}$$

The relationship between $\eta_{max}$ and *fom* is shown by Fig. 3 [22, 23].

According to (4) and (5), the optimal equivalent load resistance $R_{e\_optimal}$ is a function of the mutual inductance $M$ and the ESRs $R_1$ and $R_2$. Since $M$ is a variable that depends on the power transfer distance and it is difficult to precisely determine the values of $R_1$ and $R_2$, practical WPT systems use a tracking process to find $R_{e\_optimal}$ instead of predicting it, as shown by Fig. 4. The algorithm of the tracking is like the maximum power point tracking (MPPT) algorithm widely used in photovoltaic

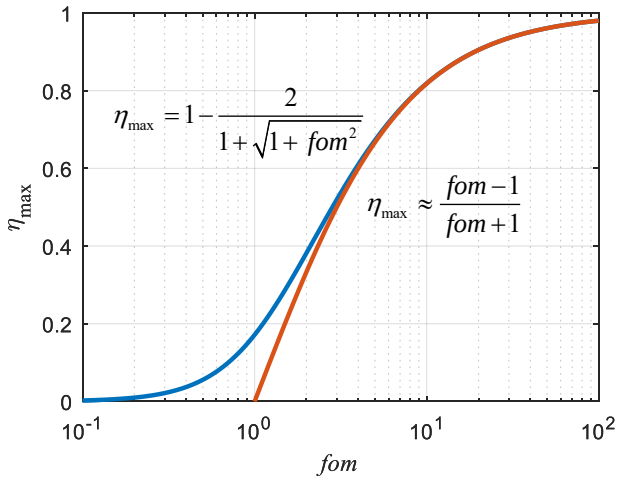


Fig. 3. $\eta_{max}$ vs. $fom$.

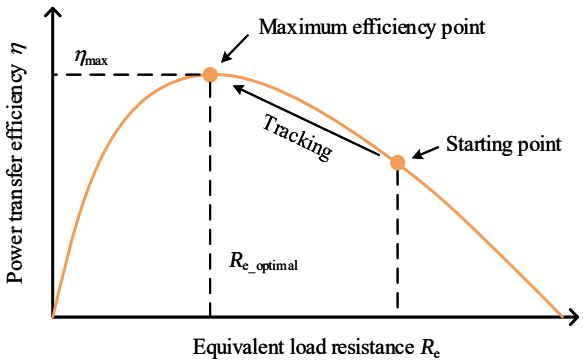


Fig. 4. Schematic diagram of MEPT.

systems, and the purpose of the tracking is to maximize the power transfer efficiency, therefore, the tracking here is called MEPT [2-4].

Since the actual load resistance of a WPT system depends on the user, the system itself must provide a control degree of freedom to convert $R_e$ to its optimal value to perform MEPT.

## III. PDM FOR MEPT

### A. Methodology

Fig. 5 shows the circuit diagram of a dual active bridge WPT system. The input and output dc voltages are denoted by $v_{in}$ and $v_o$, respectively. The half-bridge inverter in the transmitting side generates the driving voltage pulses $u_1$ and excites the transmitting side resonant current $i_1$. Through the magnetic coupling, $i_1$ induces the receiving side resonant current $i_2$. The half-bridge active rectifier in the receiving side is synchronized with $i_2$. The output of the rectifier is filtered by $C_f$ and feeds the load $R_L$. When the system is tuned in resonance, $u_1$ is in phase with $i_1$, $u_2$ is in phase with $i_2$, and the phase difference between $i_1$ and $i_2$ is 90°. The typical steady-state operating waveforms in this case are shown in Fig. 6.

The average power transferred from the transmitting side to the receiving side is

$$P = \omega_s M I_1 I_2 \tag{8}$$

where $I_1$ and $I_2$ are the root-mean-square (RMS) values of $i_1$ and

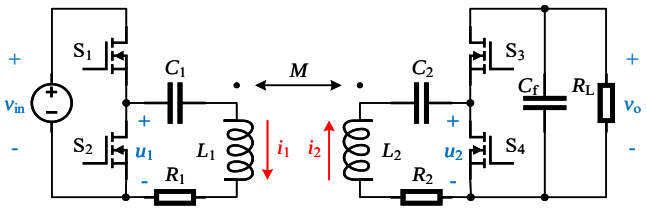


Fig. 5. Circuit diagram of a dual active bridge WPT system.

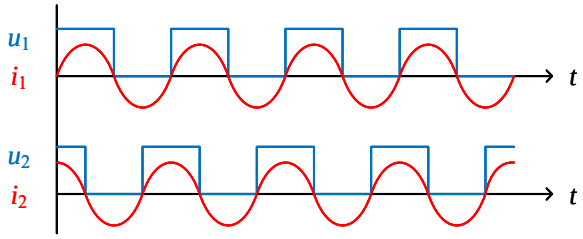


Fig. 6. Typical steady-state operating waveforms of the tuned dual active bridge WPT system.

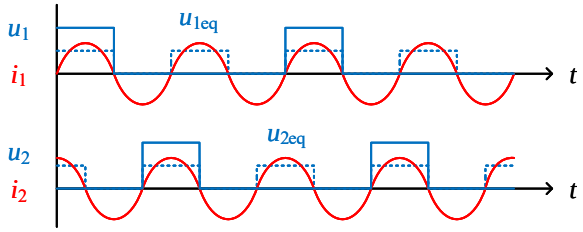


Fig. 7. Operating waveforms with PDM.

$i_2$, respectively [21]. The average input and output power are given by

$$P_{in} = \frac{\sqrt{2}}{\pi} v_{in} I_1 \tag{9}$$

and

$$P_o = \frac{\sqrt{2}}{\pi} v_o I_2 \tag{10}$$

Respectively.

Normally, the switches $S_1$ and $S_2$ of the inverter conduct alternately cycle by cycle to generate the pulses of $u_1$ continuously. However, some of the pulses can be removed by keeping $S_1$ off and $S_2$ on in a whole switching cycle, as shown in Fig. 7. For the active rectifier, some pulses of $u_2$ can be removed by keeping $S_3$ off and $S_4$ on in the same manner. The ratio of the number of remaining pulses to the number of switching cycles is called pulse density, denoted by $d$. Such kind of switching operation is called PDM.

For a loosely coupled WPT system, the energy stored in a resonator is much larger than the energy injected into or taken out from the resonator during a switching period $T_s$, i.e.

$$L_1 I_1^2 \gg P_{in} T_s > P T_s \tag{11}$$

and

$$L_2 I_2^2 \gg P T_s > P_o T_s \tag{12}$$

With the condition of (11) and (12), it is assumed that the magnitudes and phases of $i_1$ and $i_2$ are constants if the remaining pulses of $u_1$ and $u_2$ are uniformly distributed [24]. Based on this

assumption, the operation of a WPT system with PDM can be treated as a kind of quasi-steady-state operation, and a "magnitude-density balance" principle is used to analyze the operation of the system. In Fig. 7, the remaining pulses of $u_1$ and $u_2$ are represented by the solid lines, and the dashed lines represent the equivalent continuous pulses $u_{1eq}$ and $u_{2eq}$, which are balanced with $u_1$ and $u_2$. The magnitudes of $u_{1eq}$ and $u_{2eq}$ are the products of the magnitudes and pulse densities of $u_1$ and $u_2$, respectively. Therefore, the average input and output power of the system with PDM can be calculated using $u_{1eq}$ and $u_{2eq}$ and expressed as

$$P_{in} = \frac{\sqrt{2}}{\pi} d_1 v_{in} I_1 \tag{13}$$

and

$$P_o = \frac{\sqrt{2}}{\pi} d_2 v_o I_2 \tag{14}$$

where $d_1$ and $d_2$ are the pulse densities of $u_1$ and $u_2$, respectively. The equivalent load resistance $R_e$ is derived based on the power balance principle using (14) together with

$$P_o = \frac{v_o^2}{R_L} = I_2^2 R_e \tag{15}$$

and given by

$$R_e = \frac{2}{\pi^2} d_2^2 R_L \tag{16}$$

Based on (13) and (16), the system has two control degrees of freedom, i.e. $d_1$ and $d_2$, to control the power flow and convert the load resistance, respectively, and the roles of $d_1$ and $d_2$ are exchangeable as mentioned in [2] if the non-monotonic problem of post regulation can be resolved [25]. Therefore, in theory, a WPT system with dual-side PDM can regulate the output voltage and maximize the system efficiency simultaneously.

### B. *Implementation*

As mentioned above, one of the preconditions of the methodology is that the PDM pulses of $u_1$ and $u_2$ are uniformly distributed. When the required pulse density equals simple fractions, e.g. 1/2, 2/3, and 3/5, some bit patterns can be composed to generate the most uniform PDM pulses as described in [19, 26]. However, a more generic way that enables higher density resolution is the delta-sigma modulation [18, 20].

Fig. 8 shows the logics of PDM that bases on a delta-sigma modulator. The logic circuit has two input signals. One is the continuous input pulses and the other one is the specified pulse density $d$. The duty cycle of the input pulses is 50%. The rising edges of the input pulses trigger an accumulator (sigma), which accumulates the difference (delta) between $d$ and the output of a comparator. The comparator rounds the output of the accumulator to one digit. The output of the comparator is combined with the delayed input pulses by an AND gate. The output of the AND gate is the modulated output pulses. The purpose of the delay is to avoid spikes on the output pulses. As an example, Fig. 9 shows the waveforms of the modulator when $d$ = 0.7. In this scenario, ten switching cycles compose a modulation period and each modulation period contains seven output pulses. The seven output pulses are distributed as uniformly as possible.

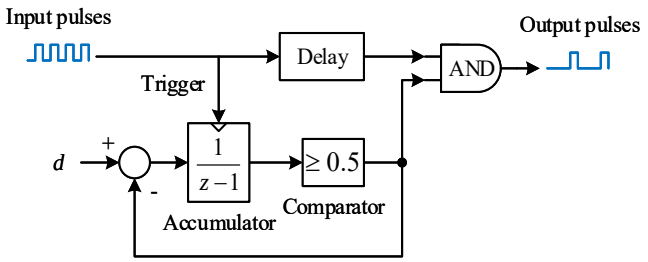


Fig. 8. Logics of the PDM based on a delta-sigma modulator.

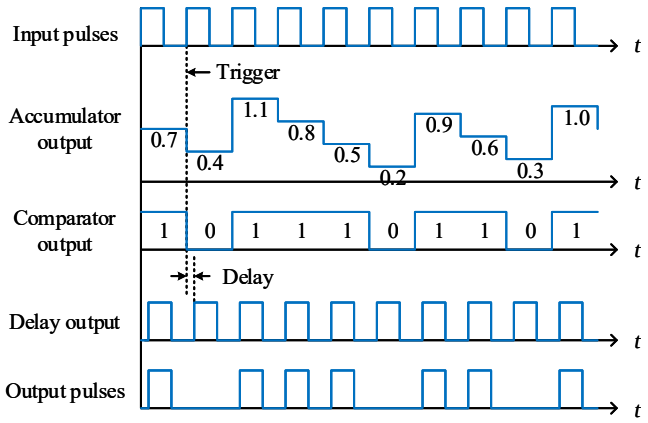


Fig. 9. Waveforms of the modulator when $d$ = 0.7.

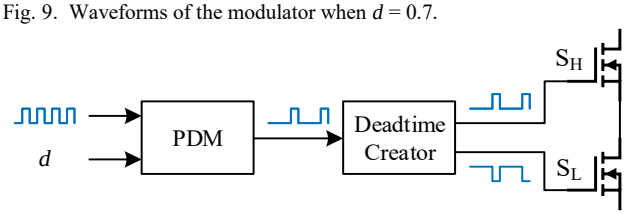


Fig. 10. Schematic of a PDM driver for a half bridge.

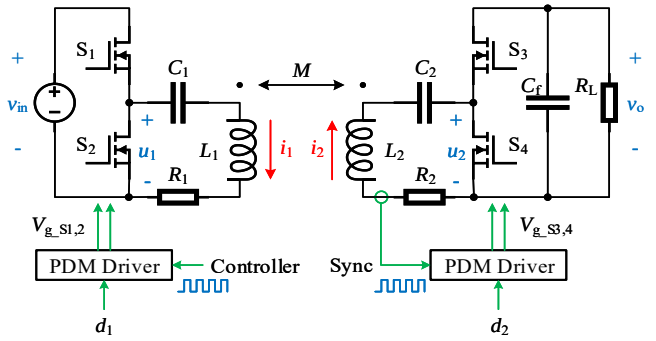


Fig. 11. Overall configuration of the proposed PDM implementation for MEPT.

Fig. 10 shows the schematic of a PDM driver for a half bridge, where $S_H$ and $S_L$ are the high side and low side switches, respectively. The PDM pulses are converted into a pair of complementary pulses with dead time by a deadtime creator so that the pulses can drive the two switches. The deadtime creator can be implemented by either sequential logics or analog circuits with a comparator [27].

Fig. 11 shows the overall configuration of the proposed PDM implementation for MEPT. The input pulses of the transmitting side PDM driver are independently generated by the

transmitting side controller, while the input pulses of the receiving side PDM driver are synchronized with $i_2$. To the best of the authors' current knowledge, this system is the most compact WPT system with the function of MEPT.

### C. Dual-Side Soft Switching

For the enhanced-mode gallium nitride (eGaN) switches, the switching loss of a hard turn-on is much greater than that of a hard turn-off [28]. Therefore, this paper focuses on the zero-voltage-switching (ZVS) of eGaN switches. The condition of the ZVS of an eGaN based half bridge is fully discharging the switch output capacitance, $C_{OSS}$, during the dead time before the switch turns on.

For the half bridges in a WPT system with PDM, this paper proposes a dual-side soft switching technique that utilizes the synchronous rectification and the coupled resonant tank to achieve the ZVS. In this technique, the reactances for ZVS on the two sides are realized by the receiving side active rectifier rather than passive components. The synchronization circuits of the active rectifier control the phase difference $\alpha_2$ between $i_2$ and $u_2$ to make $i_2$ lead $u_2$ slightly so that $i_2$ charges/discharges the $C_{OSS}$ of $S_3$ and $S_4$ during the dead time $T_{d2}$, as shown in Fig. 12, where the integral of $i_2$ during $T_{d2}$ is denoted by $Q_{ZVS2}$. The ZVS of $S_3$ and $S_4$ can be achieved when $Q_{ZVS2}$ is sufficient to charge/discharge their $C_{OSS}$ from 0V to $v_o$, or vice versa, i.e.

$$Q_{ZVS2}=\int_0^{T_{d2}} i_2\mathrm{d}t \ge \int_0^{v_o}\left(C_{OSS\_S3}+C_{OSS\_S4}\right)\mathrm{d}v \tag{17}$$

Since $i_2$ leads $u_2$, the active rectifier introduces a small equivalent capacitance into the receiving side resonant tank and therefore, the equivalent load resistance $R_e$ turns into an equivalent capacitive impedance:

$$Z_e=\frac{2}{\pi^2}d_2^{\,2}R_L\mathrm{e}^{-\mathrm{j}\alpha_2}\cos\alpha_2 \tag{18}$$

According to the ac equivalent circuit, the reflected resistance $R_r$ turns into a reflected inductive impedance $Z_r$:

$$Z_r=\frac{\left(\omega_s M\right)^2}{R_2+Z_e}\approx\frac{\left(\omega_s M\right)^2}{\left|Z_e\right|}\mathrm{e}^{\mathrm{j}\alpha_2} \tag{19}$$

The load impedance of the inverter $Z_{load\_inv}$ also turns slightly inductive:

$$Z_{load\_inv}=R_1+Z_r\approx\left|Z_r\right|\mathrm{e}^{\mathrm{j}\alpha_2} \tag{20}$$

$Z_{load\_inv}$ determines the phase difference $\alpha_1$ between $u_1$ and $i_1$:

$$\alpha_1\approx\alpha_2 \tag{21}$$

Therefore, $i_1$ lags $u_1$ slightly and charges/discharges the $C_{OSS}$ of $S_1$ and $S_2$ during the dead time $T_{d1}$, as shown in Fig. 12, where the integral of $i_1$ during $T_{d1}$ is denoted by $Q_{ZVS1}$. The ZVS of $S_1$ and $S_2$ can be achieved when $Q_{ZVS1}$ is sufficient to charge/discharge their $C_{OSS}$ from 0V to $v_{in}$, or vice versa, i.e.

$$Q_{ZVS1}=\int_0^{T_{d1}} i_1\mathrm{d}t \ge \int_0^{v_{in}}\left(C_{OSS\_S1}+C_{OSS\_S2}\right)\mathrm{d}v \tag{22}$$

To determine the minimum phase differences $\alpha_{1min}$, $\alpha_{2min}$ and the shortest dead time $T_{d1min}$, $T_{d2min}$ required by the ZVS, the waveforms of $i_1$ and $i_2$ during dead time are assumed to be part of the sin waves since the voltages across $C_{OSS}$ are much lower than the resonant voltages across $C_1$ and $C_2$. Based on this

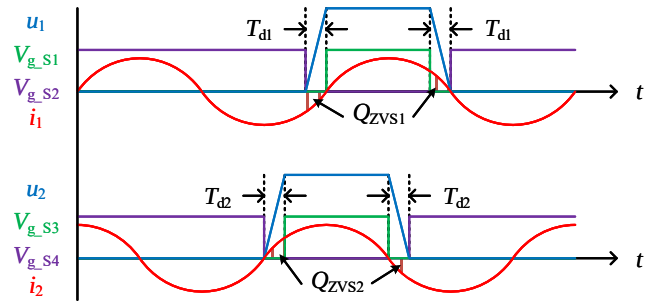


Fig. 12. Operating waveforms of the dual-side soft switching.

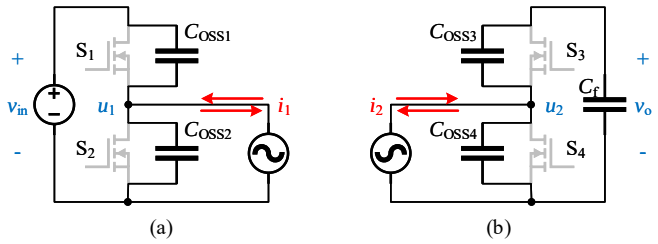


Fig. 13. Equivalent circuits during dead time (a) transmitting side, (b) receiving side.

assumption, $\alpha_{1min}$, $\alpha_{2min}$ and $T_{d1min}$, $T_{d2min}$ can be derived from (22) and (17) according to the equivalent circuits shown in Fig. 13 and expressed as

$$\alpha_{1\min}=\arccos\left(1-\frac{\sqrt{2}\pi\left(C_{OSSQ\_S1}+C_{OSSQ\_S2}\right)v_{in}}{T_s I_1}\right)\approx\sqrt{\frac{2\sqrt{2}\pi\left(C_{OSSQ\_S1}+C_{OSSQ\_S2}\right)v_{in}}{T_s I_1}} \tag{23}$$

$$T_{d1\min}=\frac{\alpha_{1\min}}{2\pi}T_s \tag{24}$$

$$\alpha_{2\min}=\arccos\left(1-\frac{\sqrt{2}\pi\left(C_{OSSQ\_S3}+C_{OSSQ\_S4}\right)v_o}{T_s I_2}\right)\approx\sqrt{\frac{2\sqrt{2}\pi\left(C_{OSSQ\_S3}+C_{OSSQ\_S4}\right)v_o}{T_s I_2}} \tag{25}$$

$$T_{d2\min}=\frac{\alpha_{2\min}}{2\pi}T_s \tag{26}$$

where $C_{OSSQ\_S1...4}$ are the charge equivalent switch output capacitances [29].

It should be noted that the dual-side soft switching technique achieves ZVS at the expense of decreased power transfer efficiency because the system is slightly detuned when $\alpha_1$ and $\alpha_2$ are not zero. Moreover, $\alpha_{1min}$ and $\alpha_{2min}$ are load dependent as indicated by (23) and (25). Fortunately, a well-designed WPT system with elaborately selected devices usually requires small $\alpha_1$ and $\alpha_2$ in a large range of load variations, and the decrease of power transfer efficiency is negligible compared to the increase of conversion efficiency.

### D. Ripple Factor of Output Voltage

The output voltage ripples are caused by the pulsed charging

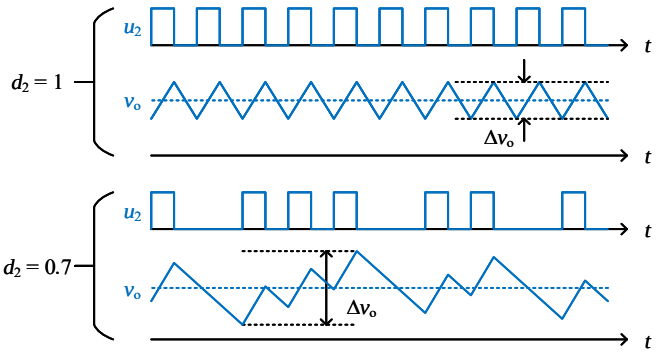


Fig. 14. Approximated waveforms of $v_o$ when $d_2 = 1$ and $d_2 = 0.7$, respectively.

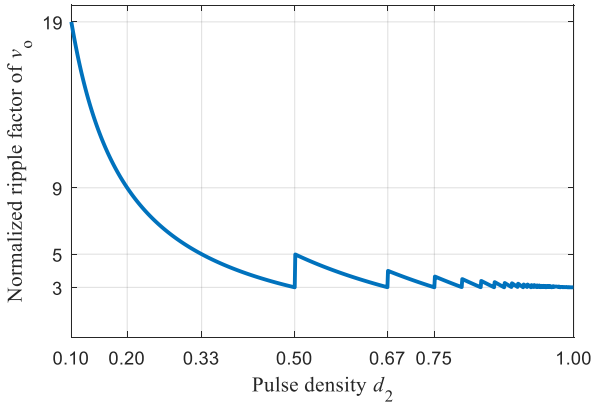


Fig. 15. Normalized ripple factor of $v_o$ vs. pulse density $d_2$.

power that charges the filter capacitor $C_f$. For example, Fig. 14 shows the approximated waveforms of $v_o$ when $d_2 = 1$ (without PDM) and $d_2 = 0.7$ (with PDM), respectively, where $v_o$ increases and decreases when $u_2$ is high ($S_3$ on, $S_4$ off) and zero ($S_3$ off, $S_4$ on), respectively.

The magnitudes of the ripples can be derived from the energy point of view. When $d_2 = 1$, the peak-valley difference of the energy stored in $C_f$ is calculated using the output power in half a switching cycle:

$$\frac{1}{2}C_f\left(v_o+\frac{1}{2}\Delta v_o\right)^2-\frac{1}{2}C_f\left(v_o-\frac{1}{2}\Delta v_o\right)^2=\frac{1}{2}T_sP_o \tag{27}$$

The ripple factor is derived from (27) and expressed as

$$\frac{\Delta v_o}{v_o}=\frac{T_s}{2R_LC_f} \tag{28}$$

When $d_2 < 1$, the maximum peak-valley difference of the energy stored in $C_f$ occurs between the beginning and the end of the longest continuous pulse segment in $u_2$, and is calculated using the charging power and the output power:

$$\begin{aligned}&\frac{1}{2}C_f\left(v_o+\frac{1}{2}\Delta v_o\right)^2-\frac{1}{2}C_f\left(v_o-\frac{1}{2}\Delta v_o\right)^2\\&=\frac{n_2}{2}T_sP_c-\left(n_2-\frac{1}{2}\right)T_sP_o\end{aligned} \tag{29}$$

where $n_2$ is the number of the pulses in the segment. According to the operation principle of the delta-sigma modulator, $n_2$ equals the smallest integer that is greater than or equal to $d_2$ / (1-$d_2$), i.e.

$$n_2=\left\lceil\frac{d_2}{1-d_2}\right\rceil \tag{30}$$

For example, when $d_2 = 0.7$, $d_2$ / (1-$d_2$) = 2.33 and $n_2 = 3$, as shown in Fig. 14. $P_c$ stands for the charging power that is derived from the power balance principle and given by:

$$P_c=\frac{2}{d_2}P_o \tag{31}$$

The ripple factor with PDM is derived from (29) and expressed as

$$\frac{\Delta v_o}{v_o}=\left(\frac{1-d_2}{d_2}\left\lceil\frac{d_2}{1-d_2}\right\rceil+\frac{1}{2}\right)\frac{T_s}{R_LC_f} \tag{32}$$

For an intuitive understanding, Fig. 15 normalizes the ripple factor of $v_o$ at various $d_2$ by setting (28) as the unit. The normalized ripple factor is always within the range of [3, 5] when $1/3 < d_2 < 1$.

## IV. Experiment

### A. Description of the Prototype

The experimental prototype is built following the schematic in Fig. 11. The coupled resonators are formed by a pair of structure-optimized coils [30] (Fig. 16) and High-Q® power capacitors (Fig. 17). The inverter and the rectifier are built based on two eGaN half-bridge modules (EPC9003C) along with two motherboards that contain the sensors and the synchronization circuits (Fig. 18). The prototype can work bi-directionally since the hardware of the two sides are identical.

The parameters of the prototype are listed in TABLE I. Both the inductances and the capacitances of the resonators on the two sides are identical, and therefore, the two resonators have the same resonant frequency, which is 0.917MHz. The switching frequency is set to be the same as the resonant frequency so that the system is tuned in resonance. The ESRs of the resonators are roughly measured and their values are close to 0.7Ω. The coupling coefficient of the two coils at 0.5m distance is about 0.01, obtained by magnetic field simulation.

### B. Effects of Voltage Regulation and Efficiency Maximization

The effects of voltage regulation and efficiency maximization of the PDM for MEPT are evaluated following the process below:

1) The experimental prototype is configured as Fig. 19. The two coils are co-axis and the face-to-face distance is 0.5m, which is 1.67 times the diameter of the resonant coils. A fixed 40V dc voltage source is used to feed the prototype and the prototype feeds a variable load resistor.

2) The PDM is disabled by setting $d_1 = d_2 = 1$. The load resistance $R_L$ is manually adjusted to an optimal value, 25Ω, so that the system efficiency from source to load is maximized to 71%. The output voltage $v_o$ at this operating point is 33V. The waveforms are shown in Fig. 20.

3) $R_L$ is manually increased from 25Ω to 100Ω with a step length of 25Ω. For each step, the prototype firstly operates without PDM, i.e. keeps $d_1 = d_2 = 1$. Then, the PDM is enabled by means of adjusting $d_2$ to maximize the efficiency for the current $R_L$ and adjusting $d_1$ to restore $v_o$ to 33V. The operating

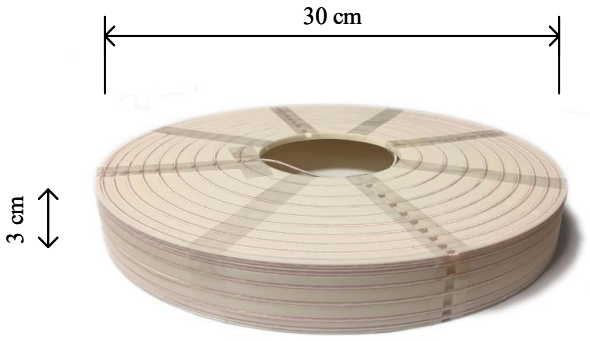


Fig. 16. Resonant coil.

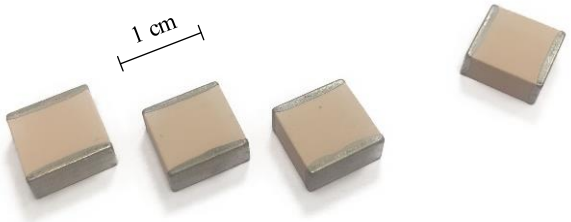


Fig. 17. Resonant caps.

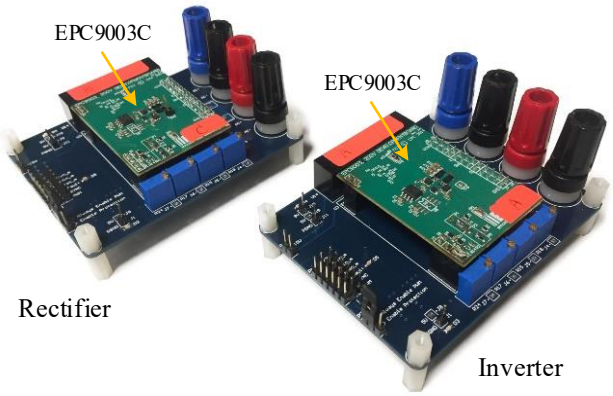


Fig. 18. Inverter and rectifier.

TABLE I
PARAMETERS OF THE EXPERIMENTAL PROTOTYPE

| Symbol | Quantity | Value |
|---|---|---|
| $L_1$ | transmitting side resonant inductance | 75.3 μH |
| $C_1$ | transmitting side resonant capacitance | 400 pF |
| $R_1$ | transmitting side ESR | ~ 0.7 Ω |
| $Q_1$ | transmitting side quality factor | ~ 620 |
| $L_2$ | receiving side resonant inductance | 75.3 μH |
| $C_2$ | receiving side resonant capacitance | 400 pF |
| $R_2$ | receiving side ESR | ~ 0.7 Ω |
| $Q_2$ | receiving side quality factor | ~ 620 |
| $f_s$ | switching frequency | 0.917 MHz |
| $k$ | coupling coefficient | 0.01 @ 0.5m |
| *fom* | figure-of-merit | ~ 6.2 @ 0.5m |
| $\eta_{max}$ | maximum theoretical efficiency | ~ 72% @ 0.5m |

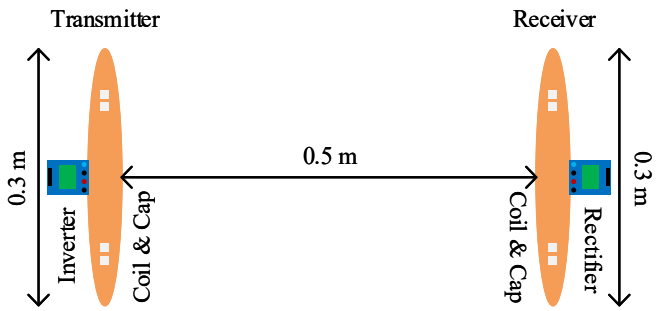


Fig. 19. Configuration of the experimental prototype.

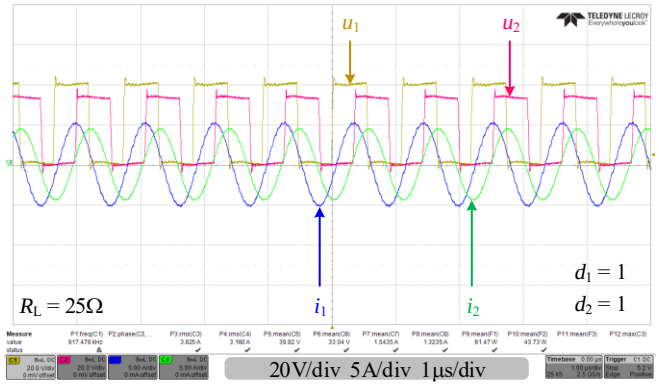


Fig. 20. Operating waveforms with the optimal load.

waveforms of all these steps are shown in Fig. 21. The output voltage and system efficiency with and without the PDM are plotted and compared in Fig. 22.

It is shown in Fig. 22 that the output voltage without PDM varies with $R_L$ and the efficiency decreases from 71% to 54% as $R_L$ increases to 4 times the optimal value. In contrast, the output voltage with PDM is always maintained at 33V and the decrease of efficiency is less than 1%. This can hardly be achieved by existing MEPT implementations.

### C. *Verification of the Soft Switching*

The operating point of Fig. 21 (d) is selected as the "worst case" to show the ZVS operation since the pulse densities of this operating point are lower than those of Fig. 21 (b) and the pulses are less uniform than those of Fig. 21 (f). The zoomed-in waveforms of Fig. 21 (d) are shown in Fig. 23. The measured phase differences are $\alpha_1 = 23.5°$ and $\alpha_2 = 21.5°$. The measured dead time are $T_{d1}$ = 50ns and $T_{d2}$ = 50ns. It can be verified according to the operating waveforms and the switch properties of EPC2010C that the phase differences and the dead time meet the requirements of (23) to (26). The soft switching of both the inverter and the rectifier is achieved and there is no spike on the voltage waveforms. Thanks to the dual-side soft switching technique, the switches do not need any heatsink or forced cooling.

### D. *Inspection of the Output Voltage Ripples*

According to Fig. 15, the normalized ripple factor of $v_o$ at the operating point of Fig. 21 (d) is the maximum among all those of the experimental operating points, therefore, Fig. 21 (d) is

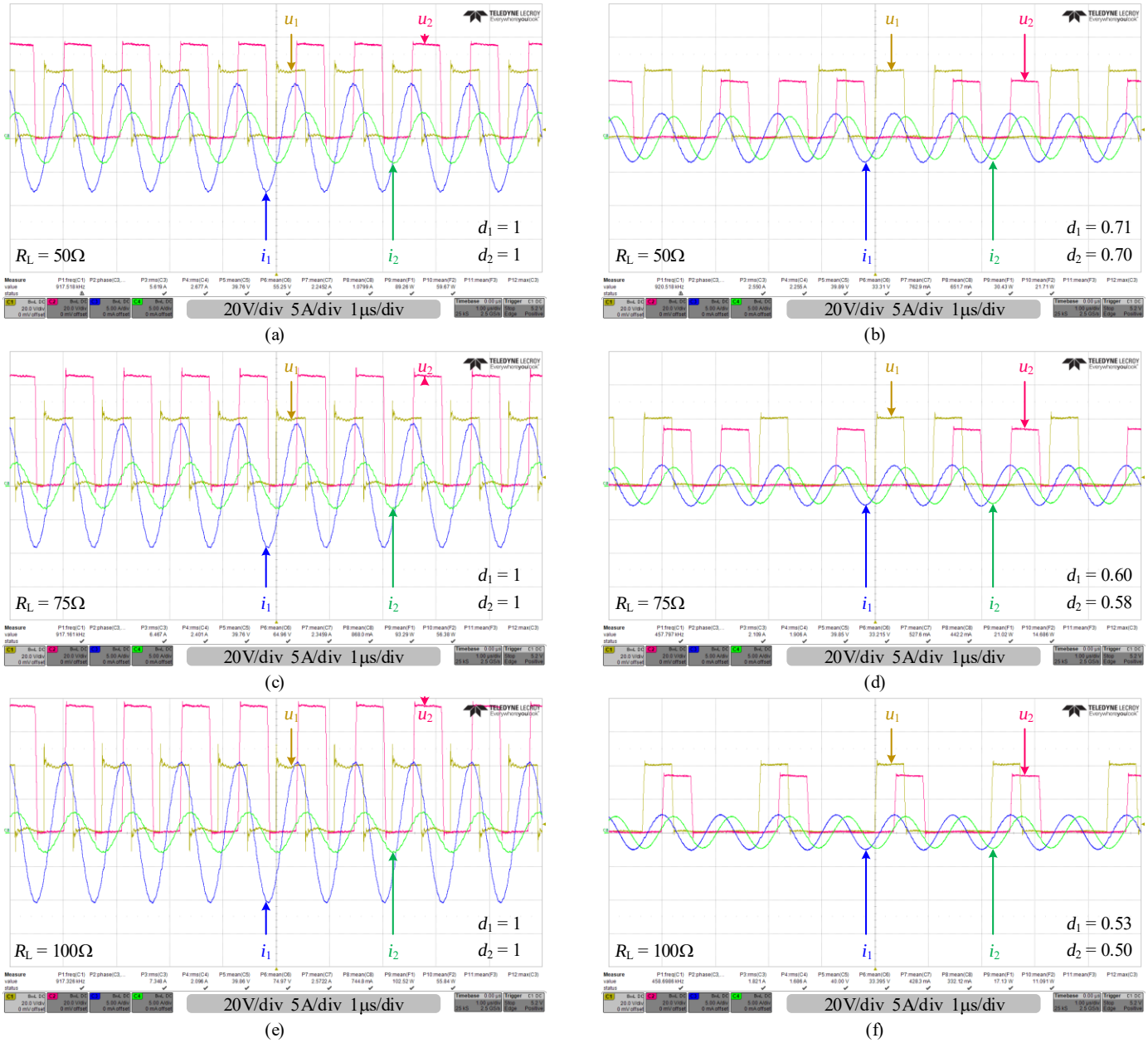


Fig. 21. Operating waveforms of (a) $R_L = 50\Omega$, w/o PDM, (b) $R_L = 50\Omega$, w/ PDM, (c) $R_L = 75\Omega$, w/o PDM, (d) $R_L = 75\Omega$, w/ PDM, (e) $R_L = 100\Omega$, w/o PDM, (f) $R_L = 100\Omega$, w/ PDM.

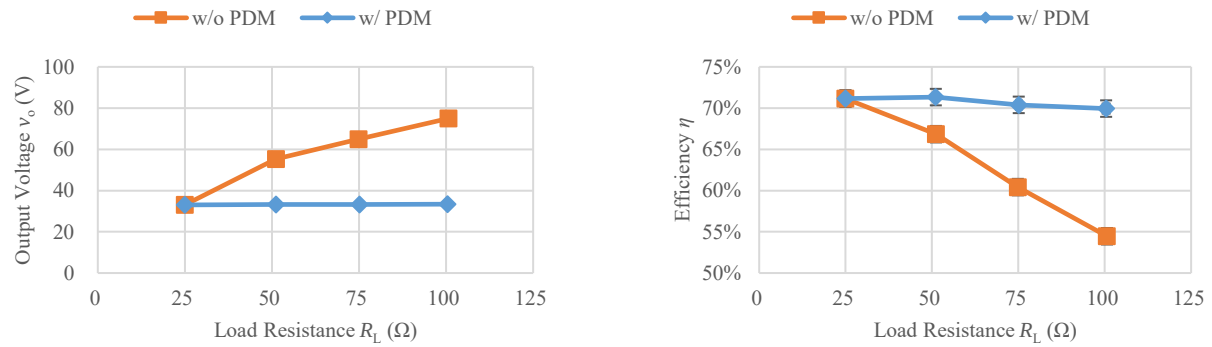


Fig. 22. Evaluation of the effects of voltage regulation and efficiency maximization.

still the "worst case". The zoomed-out waveforms of Fig. 21 (d) are shown in Fig. 24. The measured $\Delta v_o$ is 0.3V and the ripple

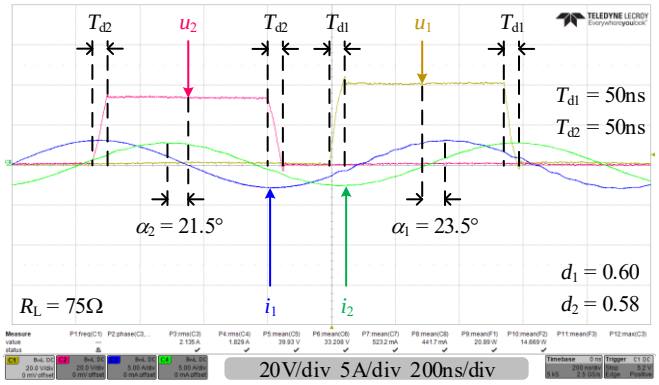


Fig. 23. Zoomed-in waveforms of Fig. 21 (d).

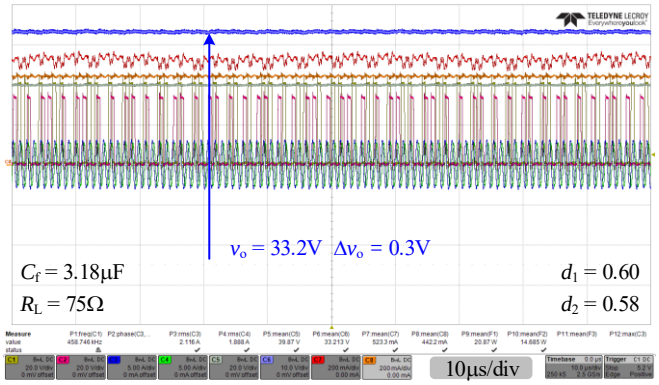


Fig. 24. Zoomed-out waveforms of Fig. 21 (d).

TABLE II
REPORTED MEPT PROTOTYPES (CHRONOLOGICAL ORDER)

| # | Frequency (MHz) | Distance (m) | Coupling coefficient | Efficiency (%) | Reference |
|---|---|---|---|---|---|
| 1 | 0.515 | 0.25 | 0.04 | 74 | [2] |
| 2 | 13.56 | 0.15 | 0.05 | 70 | [8] |
| 3 | 0.09756 | < 0.1 | 0.1 | 69 | [5] |
| 4 | 0.035 | 0.17 | 0.24 | 92 | [11] |
| 5 | 6.78 | 0.06 | 0.05 | 46 | [6] |
| 6 | 6.78 | 0.045 | 0.09 | 72 | [7] |
| 7 | 0.917 | 0.5 | 0.01 | 70 | This paper |

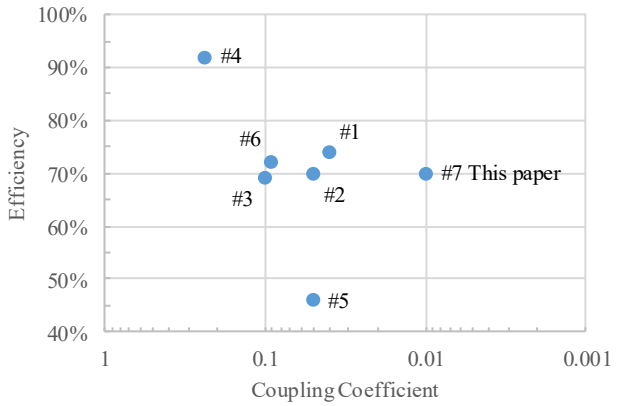


Fig. 25. Efficiency comparison of the prototypes listed in TABLE II.

factor is 0.009. The total filter capacitance $C_f$ used by the rectifier is only 3.18μF (three 0.1μF caps on EPC9003C, four 0.22μF caps and two 1μF caps on the motherboard). The theoretical ripple factor derived from (32) coincides with the measured value.

### *E. Comparison to existing MEPT techniques*

TABLE II and Fig. 25 compare the MEPT techniques reported in recent years. The key parameters of their prototypes are listed in the table. For the prototypes that operate at various power transfer distances, the operating point at the largest distance is selected and listed out. Since the coil sizes of the prototypes are quite different, the coupling coefficients are considered for a fair comparison. The listed efficiency is the source-to-load efficiency that includes power converters.

## V. CONCLUSION

This paper proposes a PDM implementation for MEPT of WPT systems as a remarkable progress compared to conventional MEPT implementations and other variants. The advantages of the proposed PDM implementation include the elimination of dc/dc converters (compared to the conventional MEPT), dual-side soft switching (compared to the phase-shift control), low output voltage ripples (compared to the on-off control), and the increased overall efficiency (especially when the coupling is very weak). By utilizing the PDM, the experimental prototype maintains constant output voltage and higher than 70% efficiency for various load resistances when the power transfer distance is 0.5m, which is 1.67 times the diameter of the coils. The limitation of the PDM is that it requires high loaded quality factors and therefore, is not very suitable for low frequency and strong coupling WPT. The future work on this topic may include the closed-loop control and tracking.

## REFERENCES

[1] H. Li, J. Fang, and Y. Tang, "Delta-sigma modulation for maximum efficiency point tracking of wireless power transfer systems," in *2017 IEEE 3rd International Future Energy Electronics Conference and ECCE Asia (IFEEC - ECCE Asia)*, 2017, pp. 434-437.

[2] H. Li, J. Li, K. Wang, W. Chen, and X. Yang, "A Maximum Efficiency Point Tracking Control Scheme for Wireless Power Transfer Systems Using Magnetic Resonant Coupling," *IEEE Transactions on Power Electronics*, vol. 30, pp. 3998-4008, Jul 2015.

[3] Y. Narusue, Y. Kawahara, and T. Asami, "Maximum Efficiency Point Tracking by Input Control for a Wireless Power Transfer System with a Switching Voltage Regulator," in *2015 IEEE Wireless Power Transfer Conference (WPTC)*, 2015.

[4] L. Q. Yuan, B. Y. Li, Y. M. Zhang, F. B. He, K. N. Chen, and Z. M. Zhao, "Maximum Efficiency Point Tracking of the Wireless Power Transfer System for the Battery Charging in Electric Vehicles," in *2015 18th International Conference on Information Fusion (Fusion)*, 2015.

[5] W. X. Zhong and S. Y. R. Hui, "Maximum Energy Efficiency Tracking for Wireless Power Transfer Systems," *IEEE Transactions on Power Electronics*, vol. 30, pp. 4025-4034, Jul 2015.

[6] T. D. Yeo, D. Kwon, S. T. Khang, and J. W. Yu, "Design of Maximum Efficiency Tracking Control Scheme for Closed-Loop Wireless Power Charging System Employing Series Resonant Tank," *IEEE Transactions on Power Electronics*, vol. 32, pp. 471-478, 2017.

[7] M. Fu, H. Yin, M. Liu, and C. Ma, "Loading and Power Control for a High-Efficiency Class E PA-Driven Megahertz WPT System," *IEEE Transactions on Industrial Electronics*, vol. 63, pp. 6867-6876, 2016.

[8] M. F. Fu, H. Yin, X. E. Zhu, and C. B. Ma, "Analysis and Tracking of Optimal Load in Wireless Power Transfer Systems," *IEEE Transactions on Power Electronics*, vol. 30, pp. 3952-3963, Jul 2015.

[9] F. C. Lee and Q. Li, "High-Frequency Integrated Point-of-Load Converters: Overview," *IEEE Transactions on Power Electronics*, vol. 28, pp. 4127-4136, 2013.

[10] S. Y. Hui, "Planar Wireless Charging Technology for Portable Electronic Products and Qi," *Proceedings of the IEEE*, vol. 101, pp. 1290-1301, 2013.

[11] T. Diekhans and R. W. De Doncker, "A Dual-Side Controlled Inductive Power Transfer System Optimized for Large Coupling Factor Variations and Partial Load," *IEEE Transactions on Power Electronics*, vol. 30, pp. 6320-6328, Nov 2015.

[12] M. Fu, H. Yin, and C. Ma, "Megahertz Multiple-Receiver Wireless Power Transfer Systems with Power Flow Management and Maximum Efficiency Point Tracking," *IEEE Transactions on Microwave Theory and Techniques*, vol. PP, pp. 1-9, 2017.

[13] S. Li and C. C. Mi, "Wireless Power Transfer for Electric Vehicle Applications," *IEEE Journal of Emerging and Selected Topics in Power Electronics*, vol. 3, pp. 4-17, 2015.

[14] G. Lovison, M. Sato, T. Imura, and Y. Hori, "Secondary-side-only simultaneous power and efficiency control for two converters in wireless power transfer system," in *Industrial Electronics Society, IECON 2015 - 41st Annual Conference of the IEEE*, 2015, pp. 004824-004829.

[15] K. Hata, T. Imura, and Y. Hori, "Dynamic wireless power transfer system for electric vehicles to simplify ground facilities - power control and efficiency maximization on the secondary side," in *2016 IEEE Applied Power Electronics Conference and Exposition (APEC)*, 2016, pp. 1731-1736.

[16] W. Zhong and S. Y. R. Hui, "Maximum Energy Efficiency Operation of Series-Series Resonant Wireless Power Transfer Systems Using On-Off Keying Modulation," *IEEE Transactions on Power Electronics*, vol. PP, pp. 1-1, 2017.

[17] Y. Sun, C. Tang, A. P. Hu, H. L. Li, and S. K. Nguang, "Multiple soft-switching operating points-based power flow control of contactless power transfer systems," *IET Power Electronics*, vol. 4, pp. 725-731, 2011.

[18] R. Shinoda, K. Tomita, Y. Hasegawa, and H. Ishikuro, "Voltage-boosting wireless power delivery system with fast load tracker by delta-sigma modulated sub-harmonic resonant switching," in *2012 IEEE International Solid-State Circuits Conference*, 2012, pp. 288-290.

[19] H. Y. Leung, D. Mccormick, D. M. Budgett, and A. P. Hu, "Pulse density modulated control patterns for inductively powered implantable devices based on energy injection control," *IET Power Electronics*, vol. 6, pp. 1051-1057, 2013.

[20] X. Li, Y. P. Li, C. Y. Tsui, and W. H. Ki, "Wireless Power Transfer System with Sigma-Delta Modulated Transmission Power and Fast Load Response for Implantable Medical Devices," *IEEE Transactions on Circuits and Systems II: Express Briefs*, vol. 64, pp. 279-283, 2017.

[21] A. Kurs, A. Karalis, R. Moffatt, J. D. Joannopoulos, P. Fisher, and M. Soljacic, "Wireless power transfer via strongly coupled magnetic resonances," *Science*, vol. 317, pp. 83-86, Jul 6 2007.

[22] H. Li, X. Yang, K. Wang, and X. Dong, "Study on efficiency maximization design principles for Wireless Power Transfer system using magnetic resonant coupling," in *ECCE Asia Downunder (ECCE Asia)*, 2013 IEEE, 2013, pp. 888-892.

[23] A. Karalis, J. D. Joannopoulos, and M. Soljačić, "Efficient wireless non-radiative mid-range energy transfer," *Annals of Physics*, vol. 323, pp. 34-48, 2008.

[24] H. Li, K. Wang, L. Huang, W. Chen, and X. Yang, "Dynamic Modeling Based on Coupled Modes for Wireless Power Transfer Systems," *IEEE Transactions on Power Electronics*, vol. 30, pp. 6245-6253, Nov 2015.

[25] H. Li, Y. Tang, K. Wang, and X. Yang, "Analysis and control of post regulation of wireless power transfer systems," in *2016 IEEE 2nd Annual Southern Power Electronics Conference (SPEC)*, 2016, pp. 1-5.

[26] J. Fang, X. Yang, L. Zhang, and Y. Tang, "An Optimal Digital Pulse-Width-Modulated Dither Technique to Enhance the Resolution of High-Frequency Power Converters," *IEEE Transactions on Power Electronics*, vol. 32, pp. 7222-7232, 2017.

[27] E. P. C. Corporation, "Development Board EPC9003C Quick Start Guide," 3rd ed.

[28] K. Wang, X. Yang, H. Li, H. Ma, X. Zeng, and W. Chen, "An Analytical Switching Process Model of Low-Voltage eGaN HEMTs for Loss Calculation," *IEEE Transactions on Power Electronics*, vol. 31, pp. 635-647, Jan 2016.

[29] M. A. d. Rooij, "The ZVS voltage-mode class-D amplifier, an eGaN FET-enabled topology for highly resonant wireless energy transfer," in *2015 IEEE Applied Power Electronics Conference and Exposition (APEC)*, 2015, pp. 1608-1613.

[30] H. Li, K. Wang, L. Huang, J. Li, and X. Yang, "Coil structure optimization method for improving coupling coefficient of wireless power transfer," in *2015 IEEE Applied Power Electronics Conference and Exposition (APEC)*, 2015, pp. 2518-2521.


**Hongchang Li** (S'12-M'16) received the B.Eng. and D.Eng. degrees in electrical engineering from Xi'an Jiaotong University, Xi'an, China, in 2011 and 2016, respectively.

From August 2014 to August 2015, he was a Visiting Scholar with the Molecular Foundry, Lawrence Berkeley National Laboratory, Berkeley, CA, USA. He is currently a Research Fellow with the Energy Research Institute at Nanyang Technological University, Singapore. His research interests include wireless power transfer, electron tomography and distributed energy storage systems.

**Jingyang Fang** (S'15) received the B.Sc. degree and the M.Sc. degree in electrical engineering from Xi'an Jiaotong University, Xi'an, China, in 2013 and 2015, respectively. He is currently working toward the Ph.D. degree at Nanyang Technological University, Singapore.

His research interests include power quality control and stability improvement of power electronics-based power system.

**Shuxin Chen** (S'17) received the B.Sc. degree in electronic engineering from the Hong Kong Polytechnic University, Hong Kong, China, in 2015, the bachelor's degree from the Sun Yet-Sen University, Guangdong, China, in 2015, and the M.Sc. degree in power electronic from Nanyang Technological University, Singapore, in 2016. He is currently working toward the Ph.D. degree in electrical and electronic engineering at Nanyang Technological University, Singapore.

His current research interests include wireless power transfer and power electronics.

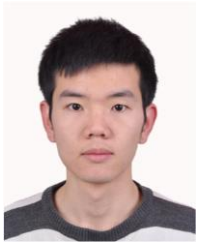

**Kangping Wang** (S'14) was born in Shaanxi, China, in 1989. He received the B.S. degree in electrical engineering from Xi'an Jiaotong University, Xi'an, China, in 2012. He is currently pursuing the Ph.D. degree in electrical engineering at Xi'an Jiaotong University.

From Sep. 2016 to Sep. 2017, he was with the Department of ePOWER, Electrical and Computer Engineering, Queen's University, Kingston, ON, Canada, as a Visiting Scholar. His research interests include power electronic integration, high frequency power conversion, and wide bandgap devices.

**Yi Tang** (S'10-M'14) received the B.Eng. degree in electrical engineering from Wuhan University, Wuhan, China, in 2007 and the M.Sc. and Ph.D. degrees from the School of Electrical and Electronic Engineering, Nanyang Technological University, Singapore, in 2008 and 2011, respectively.

From 2011 to 2013, he was a Senior Application Engineer with Infineon Technologies Asia Pacific, Singapore. From 2013 to 2015, he was a Postdoctoral Research Fellow with Aalborg University, Aalborg, Denmark. Since March 2015, he has been with Nanyang Technological University, Singapore as an Assistant Professor. He is the Cluster Director of the advanced power electronics research program at the Energy Research Institute @ NTU (ERI@N).

Dr. Tang serves as an Associate Editor for the IEEE JOURNAL OF EMERGING AND SELECTED TOPICS IN POWER ELECTRONICS. He received the Infineon Top Inventor Award in 2012.